

AirGuard: UAV and Bird Recognition Scheme for Integrated Sensing and Communications System

Hongliang Luo, Zhonghua Chu, Tengyu Zhang, Chuanbin Zhao, Bo Lin, and Feifei Gao, *Fellow, IEEE*

Abstract—In this paper, we propose an unmanned aerial vehicle (UAV) and bird recognition scheme with signal processing and deep learning for integrated sensing and communications (ISAC) system. We first provide the basic scene of low-altitude targets monitoring, and formulate the motion equations and echo signals for UAVs and birds. Next, we extract the centralized micro-Doppler (cmD) spectrum and the high resolution range profile (HRRP) of the low-altitude target from the echo signals. Then we design a dual feature fusion enabled low-altitude target recognition network with convolutional neural network (CNN), which employs both the images of cmD spectrum and HRRP as inputs to jointly distinguish between UAV and bird. Meanwhile, we generate 237600 cmD and HRRP image samples to train, validate, and evaluate the designed low-altitude target recognition network. The proposed scheme is termed as *AirGuard*, whose effectiveness has been demonstrated by simulation results.

Index Terms—Integrated sensing and communications, UAV and bird recognition, micro-Doppler spectrum, high resolution range profile (HRRP).

I. INTRODUCTION

As a coming evolution of civil aerospace commerce, low-altitude economy (LAE) refers to a comprehensive economic model that employs various air vehicles as carrier and builds multi-scenario flight activities to drive the integrated development of low-altitude production, security, operation, service and other related fields below a vertical height of one thousand meters [1]–[4]. The core elements of LAE are unmanned aerial vehicle (UAV) and manned electric vertical take-off and landing (eVTOL) [5], giving rise to plentiful activities such as low-altitude logistics, inspections, travel, surveying [6], [7].

The number of UAVs is rapidly increasing, and inevitably leads to many unrestricted and unregulated flight behaviors, which poses significant challenges to social security and privacy protection. Hence it is necessary to utilize advanced information technology to monitor all the cooperative UAVs and non-cooperative UAVs simultaneously [8]–[10]. Meanwhile, the emerging sixth generation mobile communications (6G) network is developing the integrated sensing and communications (ISAC) system, which can sense and monitor various information of the cooperative UAVs and non-cooperative UAVs with the orthogonal frequency division multiplexing (OFDM) communications signals [11]–[15].

The current version of this manuscript has been accepted by IEEE Journal on Selected Areas in Communications.

H. Luo, Z. Chu, T. Zhang, C. Zhao, B. Lin and F. Gao are with Department of Automation, Tsinghua University, Beijing 100084, China (email: luoh123@mails.tsinghua.edu.cn; c3zhua@163.com; zhang-ty22@mails.tsinghua.edu.cn; zcb23@mails.tsinghua.edu.cn; linb20@mails.tsinghua.edu.cn; feifeigao@ieee.org).

Currently, a large amount of ISAC researches focus on target detection, parameter estimation, and trajectory tracking of the UAV target. For example, Z. Xiao *et al.* propose a discrete Fourier transform (DFT) based parameter estimation method to obtain the angle, distance, and velocity of the UAV target [16]. X. Lu *et al.* apply multiple signal classification (MUSIC) algorithm to estimate the position and velocity of the UAV target [17]. R. Liu *et al.* test the performance of ISAC system in locating and tracking multiple UAVs and other targets [18]. R. Li *et al.* improve the sensing performance by optimizing target assignment and resource allocation among multiple base stations (BSs) [19]. Although these works conduct sufficient research on locating and tracking UAVs, all of them overlook a practical problem that the birds would also be illuminated by BS and thus cause echoes. Then serious false alarms will be disgustingly activated for UAV detection and monitor.

To deal with these false alarms, a natural idea is to distinguish between UAVs and birds, which is termed as *UAV and Bird Recognition* problem. Recently, J. Wei *et al.* propose a UAV feature extraction method to obtain the rotor micro-Doppler (rmD) feature caused by UAV's paddle rotation, and the sinusoidal envelope characteristics exhibited in the time-Doppler spectrum are expected to be used for the identification of rotary UAV [20]. D. Ma *et al.* evaluate the performance of UAV identification using various time-division duplex (TDD) patterns under the fifth generation mobile communications (5G) network [21]. Although these works preliminarily analyze the UAV's micro-Doppler (mD) effect with ISAC system, both of them do not distinguish between UAVs and birds.

In traditional radar areas, some researchers utilize macroscopic movements and kinematic features such as observation trajectory, velocity, acceleration, etc., of the tracked targets to distinguish between UAVs and birds [22]–[25]. Some other researchers utilize the mD effect caused by UAV's rotors to recognize UAVs and birds. For example, C. Bennett *et al.* apply fast Fourier transform (FFT) to obtain the mD spectrum of the target, and then detect the presence and the number of symmetrical peaks in each frame of mD spectrum to differentiate UAVs from other targets [26]. H. Dale *et al.* visualize the FFT based mD spectrum as an image, employ various deep learning networks to extract the hidden features from the mD image, and utilize these hidden features to classify UAVs and other targets [27]. S. Rahman *et al.* apply short time Fourier transform (STFT) to extract the mD spectrum of the target, and then recognize three different types of UAVs through GoogLeNet [28]. Besides, B. Oh *et al.* perform empirical mode decomposition (EMD) on radar echoes to obtain a set of oscillation signals, extract statistical features from them,

and utilize support vector machine (SVM) to identify UAVs and birds [29]. Moreover, as another important feature, high resolution range profile (HRRP) can reflect the distribution of scattering intensity of the extended target along the radar's line of sight, and usually contains the key structural features of the target [30]–[32]. Hence HRRP can also be used to distinguish between UAVs and birds. For example, W. Jiang *et al.* utilize long short term memory (LSTM) network to process the HRRP feature and convolutional neural network (CNN) to process the mD feature, thus realizing UAVs and other targets recognition [33]. Although these works [26]–[29], [33] provide plentiful technical reserves for UAV and bird recognition, all of them cannot be directly applied to ISAC system.

In this paper, we propose a dual feature fusion enabled UAV and bird recognition scheme with signal processing and deep learning for ISAC system. The contributions of this paper are summarized as follows.

- We formulate the motion equations and characterize the echo channels of UAVs and birds by processing their 3D mesh files and analyzing their physical motion laws. Then we compute the expressions for the echo signals of UAVs and birds under ISAC system.
- We develop a low-altitude target feature extraction method for ISAC system, in which we utilize grouped DFT to obtain the centralized micro-Doppler (cmD) spectrum of the target, and utilize DFT estimation and filtering algorithm to obtain the HRRP of the target.
- We design a dual feature fusion enabled low-altitude target recognition network with CNN, which employs both the images of cmD spectrum and HRRP as inputs to jointly recognize the UAVs and birds.
- We generate a UAV and bird echo signal dataset, and then generate 237600 cmD and HRRP image samples to train, validate, and evaluate the designed low-altitude target recognition network.
- The generated dataset and the proposed scheme are termed as *AirGuard*, whose effectiveness has been demonstrated by simulation results.

The remainder of this paper is organized as follows. In Section II, we construct the basic scene of ISAC system monitoring low-altitude targets. In Section III, we formulate the echo signals of UAVs and birds under ISAC system. In Section IV, we propose a low-altitude target recognition scheme with signal processing and deep learning. Simulation results and conclusions are given in Section V and Section VI.

Notation: Lower-case and upper-case boldface letters \mathbf{a} and \mathbf{A} denote a vector and a matrix; \mathbf{a}^* , \mathbf{a}^T and \mathbf{a}^H denote the conjugate, transpose and conjugate transpose of \mathbf{a} , respectively; $\mathbf{a}[n]$ denotes the n -th element of the vector \mathbf{a} ; $\mathbf{A}[i, j]$ denotes the (i, j) -th element of the matrix \mathbf{A} ; $\mathbf{A}[i_1 : i_2, :]$ is the submatrix composed of all columns elements in rows i_1 to i_2 of matrix \mathbf{A} ; $\mathbf{A}[:, j_1 : j_2]$ is the submatrix composed of all rows elements in columns j_1 to j_2 of matrix \mathbf{A} ; \otimes denotes the Kronecker product; \mathbb{S} denotes a set; $\text{card}(\mathbb{S})$ represents the number of elements in set \mathbb{S} ; \emptyset denotes an empty set; \cap and \cup respectively represent the intersection and union of sets; \mathbb{N}^+ denotes the positive integer space; $\|\cdot\|_2$ represents

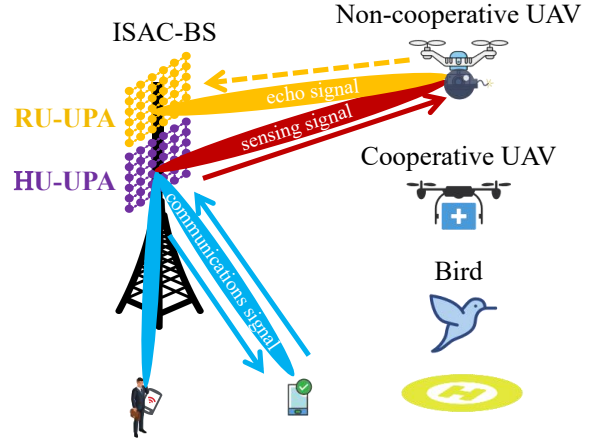


Fig. 1. ISAC scenario for low-altitude target monitoring.

the Euclidean norm.

II. SYSTEM MODEL

In this section, we provide the basic scenario of monitoring low-altitude targets with ISAC system, and derive the echo channel model for the extended targets.

A. ISAC Scene and BS Model

Fig. 1 depicts the basic scenario of monitoring low-altitude targets with ISAC system. Generally, the cooperative UAVs are obliged to report their positions, velocities, identification numbers and other information in real-time. Meanwhile, the BS can transmit sensing detection signals, receive and process the sensing echo signals to obtain various information of cooperative UAVs, non-cooperative UAVs, and birds. For conciseness, cooperative UAVs and non-cooperative UAVs are uniformly named as UAVs, and then the BS should recognize UAVs and birds by processing the sensing echo signals.

The ISAC BS employs massive MIMO arrays and OFDM signals operating in the mmWave frequency bands to realize both wireless communications and low-altitude target monitoring. As shown in Fig. 1, the BS is equipped with one hybrid unit uniform planar array (HU-UPA) and one radar unit uniform planar array (RU-UPA). The HU-UPA is responsible for transmitting downlink communications signals and receiving uplink communications signals, as well as transmitting downlink sensing signals. The RU-UPA is responsible for receiving sensing echo signals. Meanwhile, HU-UPA and RU-UPA are each equipped with $N_H = N_H^x \times N_H^z$ and $N_R = N_R^x \times N_R^z$ antenna elements, respectively, and are both vertically mounted on the 2D plane $y = 0$. The antenna spacing between the antennas along x-axis and z-axis are $d_x = d_z = d = \frac{\lambda}{2}$, where $\lambda = c/f_0$ is the wavelength, f_0 is the operating frequency of the system, and c represents the speed of light. Without loss of generality, we assume that HU-UPA and RU-UPA are co-located at the origin of the coordinate system and are parallel to each other, such that they can see the

low-altitude targets at the same propagation directions¹ [34]. We also assume that HU-UPA and RU-UPA employ the phase shifter (PS) based hybrid hardware architecture, in which a total of $N_{H,RF} \ll N_H$ and $N_{R,RF} \ll N_R$ radio frequency (RF) chains are deployed, respectively, and each antenna is connected to one PS.

Suppose that ISAC system emits OFDM signals with M subcarriers, where the lowest frequency and the subcarrier interval are f_0 and Δf , respectively. Then the transmission bandwidth is $W = M\Delta f$, and the frequency of the m -th subcarrier is $f_m = f_0 + m\Delta f$, $m = 0, 1, \dots, M - 1$. Define one OFDM frame specifically used for low-altitude target recognition as one *target recognition frame (TCF)*, which will enable idle or dedicated time-frequency resources of the BS across multiple OFDM frames in 5G new radio (NR) standard [20]. For clarity, we directly consider that one TCF contains N consecutive OFDM symbols, where the time interval between the adjacent OFDM symbols is $T_s = T'_s + T_g$, with $T'_s = \frac{1}{\Delta f}$ and T_g being the OFDM symbol duration and guard interval, respectively [35].

Let us employ the spherical coordinate (r, θ, ϕ) in 3D space, where r represents the polar distance with range $r \geq 0$, θ represents the horizontal angle with range $0^\circ \leq \theta \leq 180^\circ$, and ϕ represents the pitch angle with range $-90^\circ \leq \phi \leq 90^\circ$. Noting that BS is located at the origin of the coordinate system, we denote the service area of BS as $\{(r, \theta, \phi) | r_{min} \leq r \leq r_{max}, \theta_{min} \leq \theta \leq \theta_{max}, \phi_{min} \leq \phi \leq \phi_{max}\}$. Then we assume that all communications users and low-altitude targets are within this service area. Since the co-existence design of communications and sensing has been extensively discussed in many existing works, and the purpose of this work is low-altitude target recognition, we will ignore the communications stage and focus on how to use ISAC system to realize UAV and bird recognition.

B. Echo Channel Model of the Extended Target

The ISAC BS first transmits sensing detection signals through HU-UPA, which are then scattered by the low-altitude targets and cause echoes. These echo signals will be received by RU-UPA at the BS. To observe the detailed features of low-altitude targets, UAVs and birds should be modeled as *extended targets* that can be represented by the *multiple scattering points model*. In multiple scattering points model, the extended target could be modeled as a combination of several spatially adjacent *point targets*, and the echo channel of the extended target could be modeled as the sum of the echo channels of all corresponding point targets [36].

Let us first consider a point target with motion parameters $\{r, \theta, \phi, v_r, \omega_\theta, \omega_\phi\}$, which represent the distance, horizontal angle, pitch angle, radial velocity, horizontal angular velocity, and pitch angular velocity relative to the BS, respectively. Then the echo channel matrix of this point target on the m -th subcarrier of the n -th OFDM symbol can be represented as

$$\mathbf{H}_{n,m}^{\text{point}} = \alpha e^{-j\frac{4\pi f_m r}{c}} e^{j4\pi f_m \frac{v_r n T_s}{c}} \mathbf{a}_R(\Psi_n, \Omega_n) \mathbf{a}_H^T(\Psi_n, \Omega_n), \quad (1)$$

¹Since the communications and sensing distance is much longer than the protection distance between HU-UPA and RU-UPA, we can consider that HU-UPA and RU-UPA are located in the same position.

where α represents the channel fading factor, $\Psi_n = \Psi(\theta_n, \phi_n) = \cos \phi_n \cos \theta_n = \cos(\phi - \omega_\phi n T_s) \cos(\theta - \omega_\theta n T_s)$ represents the horizontal spatial-domain direction, $\Omega_n = \Omega(\theta_n, \phi_n) = \sin \phi_n = \sin(\phi - \omega_\phi n T_s)$ represents the pitch spatial-domain direction, $\mathbf{a}_R(\Psi, \Omega)$ and $\mathbf{a}_H(\Psi, \Omega)$ are the array steering vectors for the spatial-domain direction (Ψ, Ω) of RU-UPA and HU-UPA with the form [37], [38]

$$\mathbf{a}_R(\Psi, \Omega) = \mathbf{a}_R^x(\Psi) \otimes \mathbf{a}_R^z(\Omega) \in \mathbb{C}^{N_R \times 1}, \quad (2)$$

$$\mathbf{a}_H(\Psi, \Omega) = \mathbf{a}_H^x(\Psi) \otimes \mathbf{a}_H^z(\Omega) \in \mathbb{C}^{N_H \times 1}. \quad (3)$$

Here, \otimes denotes the Kronecker product, and

$$\mathbf{a}_R^x(\Psi) = [1, e^{j\frac{2\pi f_0 d \Psi}{c}}, \dots, e^{j\frac{2\pi f_0 d \Psi}{c} (N_R^x - 1)}]^T \in \mathbb{C}^{N_R^x \times 1}, \quad (4)$$

$$\mathbf{a}_R^z(\Omega) = [1, e^{j\frac{2\pi f_0 d \Omega}{c}}, \dots, e^{j\frac{2\pi f_0 d \Omega}{c} (N_R^z - 1)}]^T \in \mathbb{C}^{N_R^z \times 1}, \quad (5)$$

$$\mathbf{a}_H^x(\Psi) = [1, e^{j\frac{2\pi f_0 d \Psi}{c}}, \dots, e^{j\frac{2\pi f_0 d \Psi}{c} (N_H^x - 1)}]^T \in \mathbb{C}^{N_H^x \times 1}, \quad (6)$$

$$\mathbf{a}_H^z(\Omega) = [1, e^{j\frac{2\pi f_0 d \Omega}{c}}, \dots, e^{j\frac{2\pi f_0 d \Omega}{c} (N_H^z - 1)}]^T \in \mathbb{C}^{N_H^z \times 1}. \quad (7)$$

Note that Eq. (1) can be equivalently rewritten as the following set of equations

$$\begin{cases} r_n = r - v_r n T_s, \\ \theta_n = \theta - \omega_\theta n T_s, \\ \phi_n = \phi - \omega_\phi n T_s, \\ \Psi_n = \cos \phi_n \cos \theta_n, \\ \Omega_n = \sin \phi_n, \\ \mathbf{H}_{n,m}^{\text{point}} = \alpha e^{-j\frac{4\pi f_m r_n}{c}} \mathbf{a}_R(\Psi_n, \Omega_n) \mathbf{a}_H^T(\Psi_n, \Omega_n). \end{cases} \quad (8)$$

Since equations in (8) contain the motion parameters of the point target, target detection and parameter estimation tasks are typically implemented based on equations in (8) or the simplified form [39], [40]. More importantly, target detection and parameter estimation tasks typically require only a small amount of symbol observation time, and hence the velocities of the point target, i.e., v_r , ω_θ , and ω_ϕ are considered constant in existing ISAC researches. Then the motion equations of the point target in (8), i.e. $r_n = r - v_r n T_s$, $\theta_n = \theta - \omega_\theta n T_s$, and $\phi_n = \phi - \omega_\phi n T_s$ are linear equations.

However, when the ISAC system attempts to distinguish between UAVs and birds, it usually requires a longer symbol observation time. Then some scattering points in UAVs and birds will exhibit nonlinear motion such as rotation, jitter, etc. Therefore, let us rewrite the equations in (8) as

$$\begin{cases} (r_n, \theta_n, \phi_n) = g(r, \theta, \phi, v_r, \omega_\theta, \omega_\phi, n), \\ (\Psi_n, \Omega_n) = (\cos \phi_n \cos \theta_n, \sin \phi_n), \\ \mathbf{H}_{n,m}^{\text{point}} = \alpha e^{-j\frac{4\pi f_m r_n}{c}} \mathbf{a}_R(\Psi_n, \Omega_n) \mathbf{a}_H^T(\Psi_n, \Omega_n), \end{cases} \quad (9)$$

where $g(\cdot)$ represents the physical motion function. By splitting $(r_n, \theta_n, \phi_n) = g(r, \theta, \phi, v_r, \omega_\theta, \omega_\phi, n)$ into several mixed linear and nonlinear motion update steps, we can use the equations in (9) to more accurately characterize the motion details of low-altitude targets.

Based on the equations in (9), for an extended target consisting of L scattering points, the sensing echo channel of

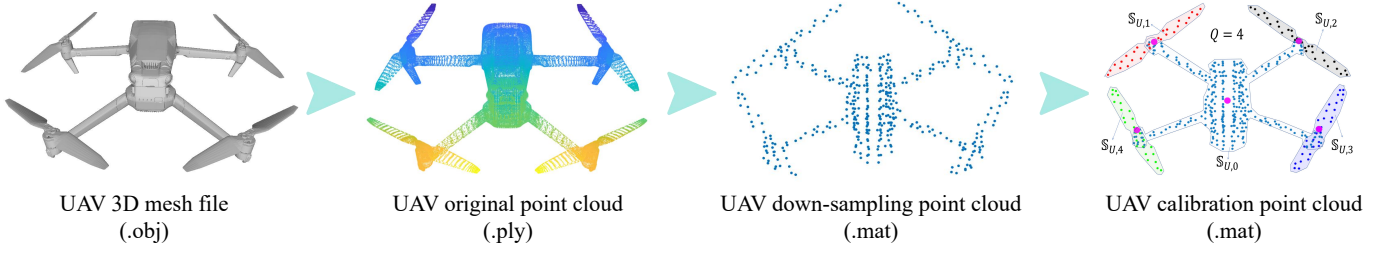


Fig. 2. Process diagram to obtain the UAV calibration point cloud.

this extended target on the m -th subcarrier of the n -th OFDM symbol can be expressed as

$$\begin{aligned} \mathbf{H}_{n,m} &= \sum_{l=1}^L \mathbf{H}_{l,n,m}^{\text{point}} \\ &= \sum_{l=1}^L \alpha_l e^{-j\frac{4\pi f_m r_{l,n}}{c}} \mathbf{a}_R(\Psi_{l,n}, \Omega_{l,n}) \mathbf{a}_H^T(\Psi_{l,n}, \Omega_{l,n}), \end{aligned} \quad (10)$$

where $r_{l,n}$, $\Psi_{l,n}$, $\Omega_{l,n}$ indicate the position information of the l -th scattering point of this extended target at the n -th symbol.

III. ECHO SIGNALS OF UAVS AND BIRDS

In this section, we formulate the motion equations and characterize the echo channels of UAVs and birds by processing their 3D mesh files and analyzing their physical motion laws. Then we compute the expressions for the echo signals of UAVs and birds under ISAC system.

A. Motion Equations and Echo Channels of the UAVs

As shown in Fig. 2, we import the 3D mesh file of the UAV (.obj file²) into the MeshLab software, an open source system that is portable and extensible for processing and editing the unstructured large 3D triangular meshes [41]. To obtain the effective point cloud that represents the skeleton of the UAV, we use the Butterfly Subdivision Surface algorithm to interpolate and refine the 3D mesh of the UAV [42]. Then we export the interpolated 3D mesh as the *original point cloud* (.ply file) of the UAV. Next, we load the original point cloud and perform uniform down-sampling on it. Then we manually calibrate the UAV's body and each paddle from the *down-sampling point cloud* to obtain the *calibration point cloud* (CPC) of the UAV. In CPC, denote the set of scattering points of the entire UAV as \mathbb{S}_U with $\text{card}(\mathbb{S}_U) = L_U$, denote the set of scattering points of the UAV's body as $\mathbb{S}_{U,0}$, and denote the set of scattering points of the UAV's each paddle as $\mathbb{S}_{U,1}, \dots, \mathbb{S}_{U,Q}$, where Q is the number of UAV's paddles with $\text{card}(\mathbb{S}_{U,i}) = L_{U,i}$, $i = 0, 1, \dots, Q$. There are $\bigcup_{i=0}^Q \mathbb{S}_{U,i} = \mathbb{S}_U$, $\mathbb{S}_{U,i} \cap \mathbb{S}_{U,j} = \emptyset$ for $i \neq j \in \{0, 1, \dots, Q\}$, and

²The ".obj file" is a plain-text file format used to define 3D geometries, including vertices, textures, and normals, commonly utilized in 3D modeling and graphics applications. The ".ply file" is a file format used to store 3D geometry data, including points, faces, and properties such as color or normals, often used in 3D scanning and modeling. The ".mat file" is a binary file format used by MATLAB to store variables, arrays, and data structures for efficient data management and analysis.

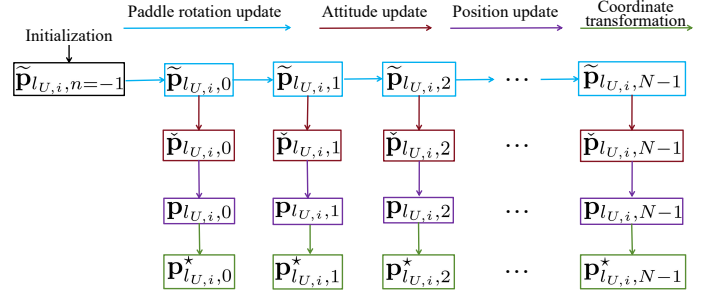


Fig. 3. Update process of UAV motion equations.

$\sum_{i=0}^Q L_{U,i} = L_U$. Meanwhile, denote the position of the $l_{U,i}$ -th scattering point in $\mathbb{S}_{U,i}$ as $\tilde{\mathbf{p}}_{l_{U,i},n=-1}$, with $i = 0, 1, \dots, Q$ and $l_{U,i} = 1, \dots, L_{U,i}$. Then the CPC of the UAV can be denoted as $\{\tilde{\mathbf{p}}_{l_{U,i},n=-1} | i = 0, 1, \dots, Q; l_{U,i} = 1, \dots, L_{U,i}\}$, whose center position is roughly located at the origin of the coordinate system.

Next, we need to analyze the motion laws of the UAV to formulate its motion equations. One of the main characteristics of UAV motion is the process of paddle rotation, which can be formulated as the scattering points in each paddle rotating around a corresponding rotation axis. Let us consider the 0-th OFDM symbol as the initial moment. We iteratively update the paddle rotation from UAV's CPC to obtain the *paddle rotation update point cloud* (PRUPC) as $\{\tilde{\mathbf{p}}_{l_{U,i},n} | i = 0, 1, \dots, Q; l_{U,i} = 1, \dots, L_{U,i}\}$, $n = 0, \dots, N-1$. Specifically, denote the initial phase and rotation frequency of the i -th paddle as $\beta_{U,i,0}$ and $F_{U,i}$, respectively, and denote the phase of paddle at the n -th symbol as $\beta_{U,i,n}$, $i = 1, \dots, Q$. We manually designate two points for the i -th paddle as the rotation axis, which are denoted as $\mathbf{p}_{U,i}^a$ and $\mathbf{p}_{U,i}^b$. Then the unit directional vector of the rotation axis is $\mathbf{e}_{U,i} = \frac{\mathbf{p}_{U,i}^a - \mathbf{p}_{U,i}^b}{\|\mathbf{p}_{U,i}^a - \mathbf{p}_{U,i}^b\|_2}$. When $n = 0, \dots, N-1$, we calculate the phase change of the i -th paddle as $\Delta\beta_{U,i,n} = \beta_{U,i,0}$ for $n = 0$, and $\Delta\beta_{U,i,n} = 2\pi F_{U,i} T_s$ for $n = 1, \dots, N-1$. Then we should rotate the point $\tilde{\mathbf{p}}_{l_{U,i},n-1}$ around the i -th rotation axis by angle $\Delta\beta_{U,i,n}$ to obtain the updated point $\tilde{\mathbf{p}}_{l_{U,i},n}$. According to the Rodrigues' rotation formula [43], $\tilde{\mathbf{p}}_{l_{U,i},n}$ can be represented as

$$\begin{aligned} \tilde{\mathbf{p}}_{l_{U,i},n} &= \mathbf{p}_{U,i}^a + \mathbf{u}_{U,i,n} \cos \Delta\beta_{U,i,n} \\ &\quad + (\mathbf{e}_{U,i} \times \mathbf{u}_{U,i,n}) \sin \Delta\beta_{U,i,n} \\ &\quad + \mathbf{e}_{U,i} (\mathbf{e}_{U,i}^T \mathbf{u}_{U,i,n}) (1 - \cos \Delta\beta_{U,i,n}), \quad i = 1, \dots, Q, \end{aligned} \quad (11)$$

with $\mathbf{u}_{U,i,n} = \tilde{\mathbf{p}}_{l_{U,i},n-1} - \mathbf{p}_{U,i}^a$. Meanwhile, the UAV's body will

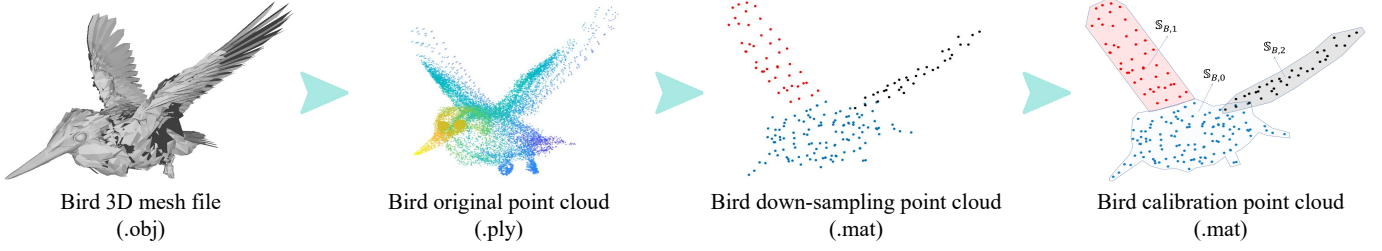


Fig. 4. Process diagram to obtain the bird calibration point cloud.

not change in PRUPC, and hence there is $\tilde{\mathbf{p}}_{l_{U,0},n} = \tilde{\mathbf{p}}_{l_{U,0},n-1}$.

Another important characteristic of UAV motion is the spatial attitude, typically described by three attitude angles, i.e., roll angle, pitch angle, and yaw angle. Meanwhile, due to the factors such as atmospheric turbulence and body vibration, the motion of UAV will exhibit significant jitter effect, mainly manifested as small-scale fluctuations in attitude angles [38]. With these motion laws, we update the attitude change from PRUPC to obtain the UAV's *attitude update point cloud* (AUPC) as $\{\tilde{\mathbf{p}}_{l_{U,i},n} | i = 0, 1, \dots, Q; l_{U,i} = 1, \dots, L_{U,i}\}$, $n = 0, \dots, N - 1$. Specifically, we denote the initial attitude and attitude jitter matrix of the UAV as $[\gamma_{U,Y,0}, \gamma_{U,P,0}, \gamma_{U,R,0}]^T$ and $\mathbf{J}_U \in \mathbb{R}^{3 \times 2}$, respectively, and then denote the attitude at the n -th symbol as $[\gamma_{U,Y,n}, \gamma_{U,P,n}, \gamma_{U,R,n}]^T$. When $n = 0, \dots, N - 1$, calculate the attitude at the n -th symbol time as $[\gamma_{U,Y,n}, \gamma_{U,P,n}, \gamma_{U,R,n}]^T = [\gamma_{U,Y,0}, \gamma_{U,P,0}, \gamma_{U,R,0}]^T + \sum_{j=0}^n [\Delta\gamma_{U,Y,n}, \Delta\gamma_{U,P,n}, \Delta\gamma_{U,R,n}]^T$, where $\Delta\gamma_{U,Y,n}, \Delta\gamma_{U,P,n}, \Delta\gamma_{U,R,n}$ are the Gaussian random numbers with mean $\mathbf{J}_U[1, 1], \mathbf{J}_U[2, 1], \mathbf{J}_U[3, 1]$ and variance $\mathbf{J}_U[1, 2], \mathbf{J}_U[2, 2], \mathbf{J}_U[3, 2]$, respectively. Then the updated point $\tilde{\mathbf{p}}_{l_{U,i},n}$ in UAV's AUPC corresponding to the point $\tilde{\mathbf{p}}_{l_{U,i},n}$ in PRUPC can be represented as

$$\tilde{\mathbf{p}}_{l_{U,i},n} = \mathbf{R}_Y(\gamma_{U,Y,n})\mathbf{R}_P(\gamma_{U,P,n})\mathbf{R}_R(\gamma_{U,R,n})\tilde{\mathbf{p}}_{l_{U,i},n}, \quad (12)$$

where

$$\mathbf{R}_Y(\gamma_{U,Y,n}) = \begin{pmatrix} \cos \gamma_{U,Y,n} & -\sin \gamma_{U,Y,n} & 0 \\ \sin \gamma_{U,Y,n} & \cos \gamma_{U,Y,n} & 0 \\ 0 & 0 & 1 \end{pmatrix}, \quad (13)$$

$$\mathbf{R}_P(\gamma_{U,P,n}) = \begin{pmatrix} \cos \gamma_{U,P,n} & 0 & \sin \gamma_{U,P,n} \\ 0 & 1 & 0 \\ -\sin \gamma_{U,P,n} & 0 & \cos \gamma_{U,P,n} \end{pmatrix}, \quad (14)$$

$$\mathbf{R}_R(\gamma_{U,R,n}) = \begin{pmatrix} 1 & 0 & 0 \\ 0 & \cos \gamma_{U,R,n} & -\sin \gamma_{U,R,n} \\ 0 & \sin \gamma_{U,R,n} & \cos \gamma_{U,R,n} \end{pmatrix}, \quad (15)$$

are the attitude rotation matrices [38].

Next, we need to update the position change from UAV's AUPC to obtain the UAV's *Cartesian coordinate position point cloud* (CCPPC) as $\{\mathbf{p}_{l_{U,i},n} | i = 0, 1, \dots, Q; l_{U,i} = 1, \dots, L_{U,i}\}$, $n = 0, \dots, N - 1$. Denote the initial position and motion velocity of the UAV as $\mathbf{p}_{U,0} = [x_{U,0}, y_{U,0}, z_{U,0}]^T$ and $\mathbf{v}_U = [v_{U,x}, v_{U,y}, v_{U,z}]^T$, respectively, and denote the position of the UAV at the n -th symbol as $\mathbf{p}_{U,n} = [x_{U,n}, y_{U,n}, z_{U,n}]^T$. When $n = 0, \dots, N - 1$, calculate the position of the UAV at the n -th

symbol as $\mathbf{p}_{U,n} = \mathbf{p}_{U,0} + nT_s\mathbf{v}_U$. Then the point $\mathbf{p}_{l_{U,i},n}$ can be represented as

$$\mathbf{p}_{l_{U,i},n} = \tilde{\mathbf{p}}_{l_{U,i},n} + \mathbf{p}_{U,n}. \quad (16)$$

Note that the spherical coordinate (r, θ, ϕ) and Cartesian coordinate (x, y, z) can be converted into each other through $x = r \cos \phi \cos \theta$, $y = r \cos \phi \sin \theta$, $z = r \sin \phi$. Here we convert the CCPPC into the *polar coordinate position point cloud* (PCPPC), denoted as $\{\mathbf{p}_{l_{U,i},n}^* = (r_{l_{U,i},n}, \theta_{l_{U,i},n}, \phi_{l_{U,i},n}) | i = 0, 1, \dots, Q; l_{U,i} = 1, \dots, L_{U,i}\}$, $n = 0, \dots, N - 1$. This PCPPC is considered as the multiple scattering points model of the UAV at the n -th OFDM symbol.

Fig. 3 summarizes the update process of the UAV motion equations. After obtaining the multiple scattering points model $\{\mathbf{p}_{l_{U,i},n}^* = (r_{l_{U,i},n}, \theta_{l_{U,i},n}, \phi_{l_{U,i},n}) | i = 0, 1, \dots, Q; l_{U,i} = 1, \dots, L_{U,i}\}$ with all N OFDM symbols, based on Eq. (10), we can characterize the sensing echo channel matrix of the UAV on the m -th subcarrier of the n -th OFDM symbol as

$$\mathbf{H}_{n,m}^{\text{UAV}} = \sum_{i=0}^Q \sum_{l_{U,i}=1}^{L_{U,i}} \alpha_{l_{U,i}} e^{-j \frac{4\pi f_m r_{l_{U,i},n}}{c}} \times \mathbf{a}_R(\Psi_{l_{U,i},n}, \Omega_{l_{U,i},n}) \mathbf{a}_H^T(\Psi_{l_{U,i},n}, \Omega_{l_{U,i},n}), \quad (17)$$

where $\Psi_{l_{U,i},n} = \cos \phi_{l_{U,i},n} \cos \theta_{l_{U,i},n}$ and $\Omega_{l_{U,i},n} = \sin \phi_{l_{U,i},n}$.

B. Motion Equations and Echo Channels of the Birds

As shown in Fig. 4, we use MeshLab to convert the 3D mesh file of the bird into the original point cloud, and then perform uniform down-sampling to obtain the down-sampling point cloud. Next we manually calibrate the bird's body and two wings to obtain the CPC of the bird, denoted as \mathbb{S}_B with card $(\mathbb{S}_B) = L_B$. Since bird only has two wings, we denote the set of scattering points of the bird's body as $\mathbb{S}_{B,0}$, and denote the set of scattering points of the bird's each wing as $\mathbb{S}_{B,1}$ and $\mathbb{S}_{B,2}$, where card $(\mathbb{S}_{B,i}) = L_{B,i}$, $i = 0, 1, 2$. There are $\bigcup_{i=0}^2 \mathbb{S}_{B,i} = \mathbb{S}_B$, $\mathbb{S}_{B,i} \cap \mathbb{S}_{B,j} = \emptyset$ for $i \neq j \in \{0, 1, 2\}$, and $\sum_{i=0}^2 L_{B,i} = L_B$. Meanwhile, denote the position of the $l_{B,i}$ -th scattering point in $\mathbb{S}_{B,i}$ as $\tilde{\mathbf{p}}_{l_{B,i},n=-1}$ with $i = 0, 1, 2$ and $l_{B,i} = 1, \dots, L_{B,i}$. Then the CPC of the bird can be denoted as $\{\tilde{\mathbf{p}}_{l_{B,i},n=-1} | i = 0, 1, 2; l_{B,i} = 1, \dots, L_{B,i}\}$, whose center position is roughly located at the origin of coordinate system.

Next, we need to analyze the motion laws of the bird to formulate its motion equations. One of the main characteristics of bird motion is the wing flapping, which can be formulated as a restricted rotation of scattering points in each wing around a corresponding rotation axis. Let us take the 0-th OFDM

$$\Delta\beta_{B,1,n} = \begin{cases} -2\beta_c F_B T_s & \Delta\beta_{B,1,n-1} > 0, \beta_{B,1,n-1} > \beta_{Bmax} \\ 2\beta_c F_B T_s & \Delta\beta_{B,1,n-1} > 0, \beta_{Bmin} < \beta_{B,1,n-1} < \beta_{Bmax} \\ 2\beta_c F_B T_s & \Delta\beta_{B,1,n-1} > 0, \beta_{B,1,n-1} < \beta_{Bmin} \\ -2\beta_c F_B T_s & \Delta\beta_{B,1,n-1} < 0, \beta_{B,1,n-1} > \beta_{Bmax} \\ -2\beta_c F_B T_s & \Delta\beta_{B,1,n-1} < 0, \beta_{Bmin} < \beta_{B,1,n-1} < \beta_{Bmax} \\ 2\beta_c F_B T_s & \Delta\beta_{B,1,n-1} < 0, \beta_{B,1,n-1} < \beta_{Bmin} \end{cases} \quad (18)$$

symbol time as the initial moment. We iteratively update the wing flapping from the CPC of bird to obtain the *wing flapping update point cloud* (WFUPC) as $\{\tilde{\mathbf{p}}_{l_{B,i},n} | i = 0, 1, 2; l_{B,i} = 1, \dots, L_{B,i}\}$, $n = 0, \dots, N - 1$. Specifically, assume that the two wings of a bird remain symmetrical. Denote the initial phase and flapping frequency of the wings as $\beta_{B,i,0}$ and F_B , respectively, and denote the wings' phase at the n -th symbol as $\beta_{B,i,n}$. Denote the maximum and minimum angles that can be achieved during wing flapping as β_{Bmax} and β_{Bmin} . We manually designate two points for the i -th wing as the rotation axis of wing flapping, which are denoted as $\mathbf{p}_{B,i}^a$ and $\mathbf{p}_{B,i}^b$, $i = 1, 2$. In the same coordinate system, the rotation directions of the two wings are opposite.

Without loss of generality, we only elaborate on the flapping process of $S_{B,1}$ here, whose flapping frequency and rotation axis direction are F_B and $\mathbf{e}_{B,1} = \frac{\mathbf{p}_{B,1}^a - \mathbf{p}_{B,1}^b}{\|\mathbf{p}_{B,1}^a - \mathbf{p}_{B,1}^b\|_2}$. When $n = 0$, we calculate the phase change of the wing as $\Delta\beta_{B,1,n} = \beta_{B,1,0}$. When $n \neq 0$, we calculate $\Delta\beta_{B,1,n}$ as shown in Eq. (18) at the top of this page, where $\beta_c = \beta_{Bmax} - \beta_{Bmin} > 0$ and $\beta_{B,1,n} = \beta_{B,1,n-1} + \Delta\beta_{B,1,n-1}$. Then we should rotate the point $\tilde{\mathbf{p}}_{l_{B,1},n-1}$ around the 1-st rotation axis by angle $\Delta\beta_{B,1,n}$ to obtain the updated point $\tilde{\mathbf{p}}_{l_{B,1},n}$. According to Rodrigues' rotation formula [43], $\tilde{\mathbf{p}}_{l_{B,1},n}$ can be represented as

$$\begin{aligned} \tilde{\mathbf{p}}_{l_{B,1},n} &= \mathbf{p}_{B,1}^a + \mathbf{u}_{l_{B,1},n} \cos \Delta\beta_{B,1,n} \\ &\quad + (\mathbf{e}_{B,1} \times \mathbf{u}_{l_{B,1},n}) \sin \Delta\beta_{B,1,n} \\ &\quad + \mathbf{e}_{B,1} (\mathbf{e}_{B,1}^T \mathbf{u}_{l_{B,1},n}) (1 - \cos \Delta\beta_{B,1,n}), \end{aligned} \quad (19)$$

where $\mathbf{u}_{l_{B,1},n} = \tilde{\mathbf{p}}_{l_{B,1},n-1} - \mathbf{p}_{B,1}^a$. Similarly, we can formulate $\tilde{\mathbf{p}}_{l_{B,2},n}$. Meanwhile, since the body of the bird will not change in WFUPC, there is $\tilde{\mathbf{p}}_{l_{B,0},n} = \tilde{\mathbf{p}}_{l_{B,0},n-1}$.

Similar to the motion equations of the UAV, we also need to formulate the bird's attitude update, position update, and coordinate transformation based on the bird's WFUPC. Denote the initial attitude and attitude jitter matrix of the bird as $[\gamma_{B,Y,0}, \gamma_{B,P,0}, \gamma_{B,R,0}]^T$ and $\mathbf{J}_B \in \mathbb{R}^{3 \times 2}$, respectively, and denote the attitude at the n -th symbol as $[\gamma_{B,Y,n}, \gamma_{B,P,n}, \gamma_{B,R,n}]^T$. Meanwhile, denote the initial position and motion velocity of the bird as $\mathbf{p}_{B,0}$ and \mathbf{v}_B , respectively, and denote the position of the bird at the n -th symbol as $\mathbf{p}_{B,n}$. Note that the bird's attitude update, position update, and coordinate transformation are completely consistent with the UAV. Therefore, Similar to Eq. (12) and Eq. (16), we can ultimately obtain the multiple scattering points model of the bird as $\{\mathbf{p}_{l_{B,i},n}^* = (r_{l_{B,i},n}, \theta_{l_{B,i},n}, \phi_{l_{B,i},n}) | i = 0, 1, 2; l_{B,i} = 1, \dots, L_{B,i}\}$, $n = 0, \dots, N - 1$.

Then based on Eq. (10), we can characterize the sensing echo channel matrix of the bird on the m -th subcarrier of the

n -th OFDM symbol as

$$\mathbf{H}_{n,m}^{\text{bird}} = \sum_{i=0}^2 \sum_{l_{B,i}=1}^{L_{B,i}} \alpha_{l_{B,i}} e^{-j \frac{4\pi f_m r_{l_{B,i},n}}{c}} \times \mathbf{a}_R(\Psi_{l_{B,i},n}, \Omega_{l_{B,i},n}) \mathbf{a}_H^T(\Psi_{l_{B,i},n}, \Omega_{l_{B,i},n}), \quad (20)$$

where $\Psi_{l_{B,i},n} = \cos \phi_{l_{B,i},n} \cos \theta_{l_{B,i},n}$ and $\Omega_{l_{B,i},n} = \sin \phi_{l_{B,i},n}$.

C. Echo Signals of UAVs and Birds

Assuming that the BS performs beamforming through HU-UPA. The transmission signal on the m -th subcarrier of the n -th OFDM symbol is

$$\mathbf{x}_{n,m} = \sqrt{\frac{\rho_s P_t}{N_H}} \mathbf{a}_H(\Psi_t, \Omega_t) s_{n,m}, \quad (21)$$

where P_t is the transmission power of BS, ρ_s is the power allocation factor towards the sensing direction, (Ψ_t, Ω_t) is the beamforming direction of HU-UPA, and $s_{n,m}$ is the sensing detection signal. Meanwhile, assume that RU-UPA of the BS also performs receive beamforming with $\mathbf{w}_{n,m} = \sqrt{\frac{1}{N_R}} \mathbf{a}_R(\Psi_r, \Omega_r)$. Then the frequency-domain echo signal received by BS on the m -th subcarrier of the n -th symbol can be represented as

$$y_{n,m} = \mathbf{w}_{n,m}^H \mathbf{H}_{n,m}^{\text{target}} \mathbf{x}_{n,m}^* + n_{n,m}, \quad (22)$$

where $\mathbf{H}_{n,m}^{\text{target}} = \mathbf{H}_{n,m}^{\text{UAV}}$ when the target is a UAV, while $\mathbf{H}_{n,m}^{\text{target}} = \mathbf{H}_{n,m}^{\text{bird}}$ when the target is a bird. Moreover, $n_{n,m}$ is zero-mean additive Gaussian noise with variance σ^2 .

We command the transmitting beam direction and receiving beam direction of the BS to directly point towards the initial direction of the UAV or the bird. After receiving the echo signal $y_{n,m}$, we erase the influence of $s_{n,m}$ and obtain

$$\tilde{y}_{n,m} = y_{n,m} / s_{n,m}. \quad (23)$$

Then we concatenate the echo signals on all subcarriers and all OFDM symbols into a matrix $\mathbf{Y} \in \mathbb{C}^{N \times M}$, where $\mathbf{Y}[n, m] = y_{n,m}$, $n = 0, \dots, N - 1$, and $m = 0, \dots, M - 1$.

IV. DUAL FEATURE FUSION ENABLED LOW-ALTITUDE TARGET RECOGNITION SCHEME

In this section, we develop the low-altitude target feature extraction method to obtain the cmD spectrum and HRRP of the target, and then design a dual feature fusion enabled low-altitude target recognition network with CNN to distinguish between UAVs and birds.

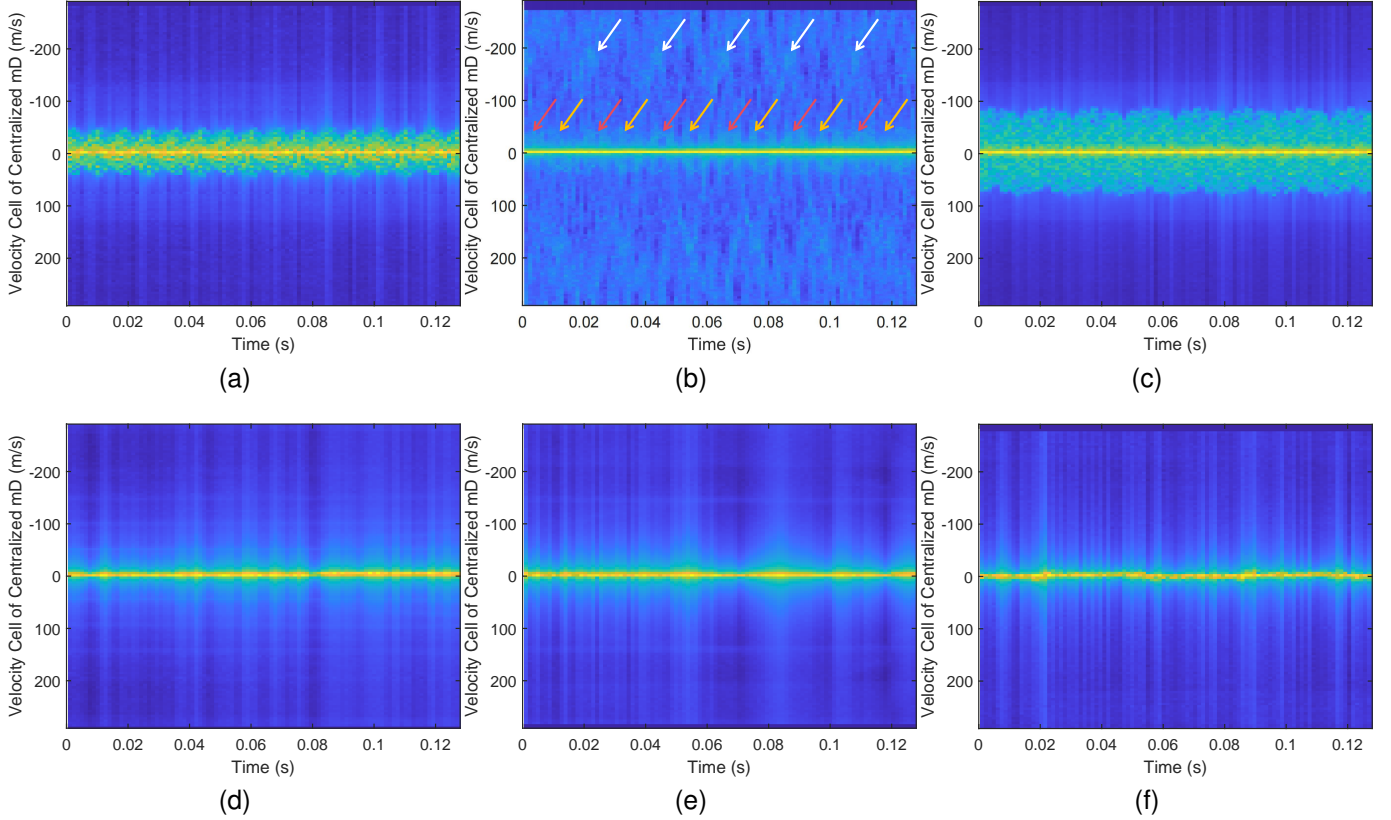


Fig. 5. Centralized micro-Doppler spectrum of six different targets. (a) DJI MAVIC 3, a four rotor UAV. (b) Ehang eVTOL, an eight rotor UAV. (c) Six Rotor UAV, a six rotor UAV. (d) Crow. (e) Pigeon. (f) Sparrow. $f_0 = 26$ GHz, $\Delta f = 480$ kHz, $M = 4096$, $T_s = 10$ us, $N = 12800$, $N_0 = 128$, $G = 100$.

A. cmD Spectrum of Low-Altitude Target

Let us divide N OFDM symbols into G groups, each containing N_0 symbols with $G, N_0, N \in \mathbb{N}^+$ and $N = GN_0$. We then extract the submatrix corresponding to the g -th group from the echo signals \mathbf{Y} as $\mathbf{Y}_g = \mathbf{Y}[(g-1)N_0 + 1 : gN_0, :] \in \mathbb{C}^{N_0 \times M}$ with $g = 1, 2, \dots, G$. It can be inferred from Eq. (17), Eq. (20), Eq. (22) and Eq. (23) that \mathbf{Y}_g contains the distance and velocity information for all scattering points of the low-altitude target. Hence we perform velocity DFT on \mathbf{Y}_g , i.e., perform N_0 points DFT on each column of \mathbf{Y}_g to obtain $\mathbf{Y}_{g,a}$ as

$$\mathbf{Y}_{g,a}[n_0, m] = \sum_{i_0=0}^{N_0-1} \mathbf{Y}_g[i_0, m] e^{-j \frac{2\pi i_0}{N_0} n_0}, \quad (24)$$

with $n_0 = 0, \dots, N_0 - 1$ and $m = 0, \dots, M - 1$. Since the target's velocity possesses both positive and negative values, we move the zero frequency component of each column in $\mathbf{Y}_{g,a}$ to the center of each column, and obtain

$$\mathbf{Y}_{g,b}[n_0, m] = \mathbf{Y}_{g,a}[(n_0 + \lfloor N_0/2 \rfloor) \bmod N_0, m], \quad (25)$$

where $\lfloor \cdot \rfloor$ represents the floor function, and mod represents the remainder function. Then we perform distance inverse discrete Fourier transform (IDFT) on $\mathbf{Y}_{g,b}$, that is, perform M point

IDFT on each row of $\mathbf{Y}_{g,b}$ to obtain the distance-velocity spectrum as

$$\mathbf{Y}_{g,c}[n_0, m_0] = \frac{1}{M} \sum_{i_0=0}^{M-1} \mathbf{Y}_{g,b}[n_0, i_0] e^{j \frac{2\pi i_0}{M} m_0}, \quad (26)$$

with $m_0 = 0, \dots, M - 1$ and $n_0 = 0, \dots, N_0 - 1$. Next, we take the modulus values of $\mathbf{Y}_{g,c}$ to obtain $\mathbf{Y}_{g,d}$ with $\mathbf{Y}_{g,d}[n_0, m_0] = \text{abs}\{\mathbf{Y}_{g,c}[n_0, m_0]\}$, where $\text{abs}\{\cdot\}$ represents taking the modulus value. We sum up all the elements in each row of $\mathbf{Y}_{g,d}$ to obtain the mD spectrum slice for the g -th time period as

$$\mathbf{y}_{g,\text{mD}} = \sum_{m=0}^{M-1} \mathbf{Y}_{g,d}[:, m] \in \mathbb{R}^{N_0 \times 1}, \quad (27)$$

which contains all the mD information of the low-altitude targets from the $(g-1)N_0$ -th symbol to the (gN_0-1) -th symbol. Then we concatenate the mD spectrum slices of all G groups together to obtain the mD spectrum matrix as

$$\mathbf{Y}_{\text{mD}} = [\mathbf{y}_{1,\text{mD}}, \mathbf{y}_{2,\text{mD}}, \dots, \mathbf{y}_{G,\text{mD}}] \in \mathbb{R}^{N_0 \times G}. \quad (28)$$

Note that different velocities of the target will affect the central index of the mD spectrum, which in turn affect the generalization of subsequent target recognition. Hence we shift the Doppler unit where the target's velocity is located to the center row of \mathbf{Y}_{mD} . For this purpose, let us calculate the index of the Doppler unit where the target velocity is located as

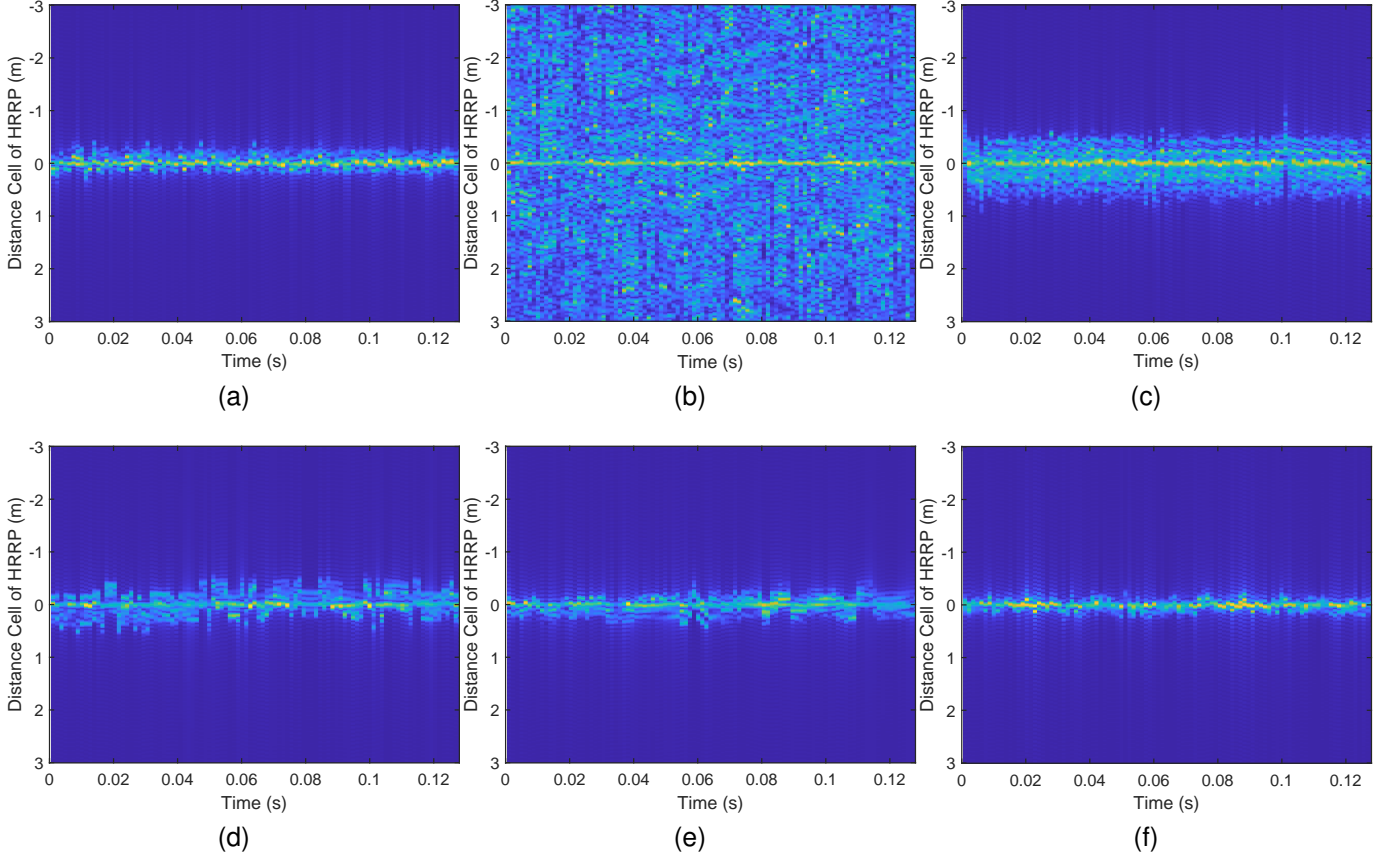


Fig. 6. HRRP temporal sequence of six different targets. (a) DJI MAVIC 3. (b) Ehang eVTOL. (c) Six Rotor UAV. (d) Crow. (e) Pigeon. (f) Sparrow. $f_0 = 26$ GHz, $\Delta f = 480$ kHz, $M = 4096$, $T_s = 10$ us, $N = 12800$, $N_0 = 128$, $G = 100$, $[-r_{\text{HRRP},\min}, r_{\text{HRRP},\max}] = [-3m, 3m]$, $\Delta r_{\text{HRRP}} = 0.01m$.

$n_0^* = \arg \max_{n_0} \sum_{g=1}^G \mathbf{y}_{g,\text{mD}}$. Then the cmD spectrum matrix can be represented as

$$\mathbf{Y}_{\text{mD}}^{\text{center}} = \frac{\mathbf{Y}_{\text{mD}}^{\text{extend}} [n_0^* - \lfloor \frac{N_0}{2} \rfloor + 1 : n_0^* + \lfloor \frac{N_0}{2} \rfloor, :]}{\max\{\mathbf{Y}_{\text{mD}}\}} \in \mathbb{R}^{N_0 \times G}, \quad (29)$$

where $\mathbf{Y}_{\text{mD}}^{\text{extend}} = [\mathbf{0}_{N_0 \times G}^T, \mathbf{Y}_{\text{mD}}^T, \mathbf{0}_{N_0 \times G}^T]^T \in \mathbb{R}^{3N_0 \times G}$, and $\max\{\cdot\}$ represents the function of finding the maximum value.

Fig. 5 shows the cmD spectrum of six different low-altitude targets, including DJI MAVIC 3, Ehang eVTOL, Six Rotor UAV, crow, pigeon, and sparrow. The specific information of these low-altitude targets can be seen in Fig. 8 in the subsequent simulations section. It can be seen from Fig. 5(a) and Fig. 5(c) that the cmD spectrums of the four rotor UAV and the six rotor UAV exhibit obvious sine envelope, which corresponds to the high frequency rotation of the UAVs' paddles. Besides, since the size of Ehang eVTOL is much larger than that of typical UAVs, the multi-layered sine envelopes appear in the cmD spectrum as shown in Fig. 5(b), which is different from other UAVs. In addition, it can be seen from Fig. 5(d), Fig. 5(e) and Fig. 5(f) that only a sinusoidal envelope with slower frequency and lower amplitude can be seen in the cmD spectrum of the birds within a limited observation time, and even the sinusoidal envelope cannot be seen in the cmD spectrum of most birds. This phenomenon is mainly due to that the frequency of bird flapping wings is relatively low.

Therefore, we can save the cmD spectrum of low-altitude targets as images for subsequent target recognition.

B. HRRP Sequence Spectrum of Low-Altitude Target

To obtain the HRRP of low-altitude target with low complexity, we extract the echo signal vector of the target at the $((g-1)N_0 + 1)$ -th OFDM symbol from \mathbf{Y} as $\mathbf{y}_g = \{\mathbf{Y}[(g-1)N_0 + 1, :]\}^T \in \mathbb{C}^{M \times 1}$, where $g = 1, \dots, G$. Then we perform M point distance IDFT on \mathbf{y}_g to obtain $\mathbf{y}_{g,a}$ with

$$\mathbf{y}_{g,a}[m_0] = \frac{1}{M} \sum_{i_0=0}^{M-1} \mathbf{y}_g[i_0] e^{j \frac{2\pi i_0}{M} m_0}, \quad (30)$$

where $m_0 = 0, \dots, M-1$. Then we take the modulus values of $\mathbf{y}_{g,a}$ to obtain $\mathbf{y}_{g,b}$ with $\mathbf{Y}_{g,b}[m_0] = \text{abs}\{\mathbf{Y}_{g,a}[m_0]\}$. By calculating the index number of the maximum value in $\mathbf{y}_{g,b}$ as $m_{0,g}^* = \arg \max_{m_0} \mathbf{y}_{g,b}$, we can obtain the distance estimation

result of the target in the g -th group as $\hat{r}_g = \frac{c(m_{0,g}^* - 1)}{2W}$. Then we construct a distance search vector as $\mathbf{r}_g = (\hat{r}_g - r_{\text{HRRP},\min} : \Delta r_{\text{HRRP}} : \hat{r}_g + r_{\text{HRRP},\max})^T$, where $(\zeta_1 : \Delta \zeta : \zeta_2)^T$ represents constructing a column vector with ζ_1 as the initial value, $\Delta \zeta$ as the step size, and ζ_2 as the termination value. Moreover, Δr_{HRRP} and $[-r_{\text{HRRP},\min}, r_{\text{HRRP},\max}]$ are the resolution and range of HRRP set by the system, respectively. Denote the length of \mathbf{r}_g as $\text{len}(\mathbf{r}_g)$, and there

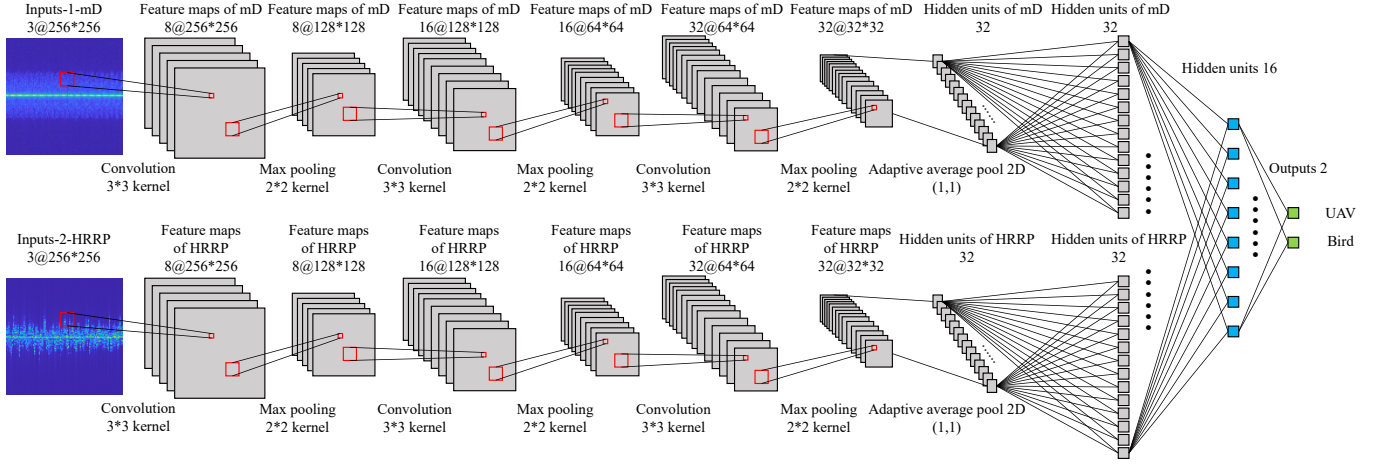


Fig. 7. Low-altitude target recognition network based on convolutional neural network combined with micro-Doppler spectrum and HRRP.

should be $\text{len}(\mathbf{r}_g) \equiv \frac{r_{\text{HRRP,max}} + r_{\text{HRRP,min}} + \Delta r_{\text{HRRP}}}{\Delta r_{\text{HRRP}}} \triangleq I$. For each element $\mathbf{r}_g[i]$ in \mathbf{r}_g , we construct a dictionary vector as $\mathbf{a}_{g,i} \in \mathbb{C}^{M \times 1}$ with $\mathbf{a}_{g,i}[m] = e^{-j4\pi \frac{f_m \mathbf{r}_g[i]}{c}}$, where $i = 1, \dots, I$ and $m = 0, \dots, M - 1$. Let us calculate the matching value corresponding to $\mathbf{r}_g[i]$ as

$$G_{g,i} = \text{abs}\{\mathbf{a}_{g,i}^H \mathbf{y}_{g,a}\}. \quad (31)$$

Then we stack $\{G_{g,i} | i = 1, \dots, I; g = 1, \dots, G\}$ into a matrix and obtain the HRRP sequence spectrum matrix of the low-altitude target as $\mathbf{Y}_{\text{HRRP}} \in \mathbb{R}^{I \times G}$ with $\mathbf{Y}_{\text{HRRP}}[i, g] = G_{g,i}$.

Fig. 6 shows the HRRP sequence spectrum of six different low-altitude targets, also including DJI MAVIC 3, Ehang eVTOL, Six Rotor UAV, crow, pigeon, and sparrow. It is seen from Fig. 6(b) that Ehang eVTOL shows significant broadening throughout the entire HRRP range of $[-3m, 3m]$. The reason is that the size of Ehang eVTOL is much larger than other UAVs and birds. Besides, since the rotation frequency of the UAV's paddles is much higher than the wing frequency of ordinary birds, the HRRP broadening of the six rotor UAV is more continuous as can be seen from Fig. 6(c), Fig. 6(d), and Fig. 6(e), which will help distinguish between UAVs and birds. From Fig. 6(a), Fig. 6(d), and Fig. 6(e), it can be found that the HRRP of DJI MAVIC 3 possesses more obvious periodicity than that of crow and pigeon. However, this phenomenon is not obvious for DJI MAVIC 3 and sparrow. Therefore, although HRRP can help distinguish between UAVs and birds, the gain may be limited for some specific low-altitude targets.

C. Low-Altitude Target Recognition Network

We next design a dual feature fusion enabled low-altitude target recognition network with CNN as shown in Fig. 7. The inputs of the low-altitude target recognition network are two RGB color images with dimensions of $3@256 \times 256$. Here “3@” represents the number of channels of the image, and “ 256×256 ” represents the data dimensions in each image channel. These two images respectively depict the visualization results of the target's cmD spectrum and HRRP sequence spectrum. The cmD image and HRRP image are processed through three convolutional layers with the kernel

size 3×3 and three max-pooling layers with the kernel size 2×2 , respectively, to obtain the deep feature maps with the size $32@32 \times 32$. Then we utilize the adaptive average pooling to transform the deep feature maps into 32 hidden units, which are then transformed into 32 new hidden units through a fully connected layer. Next we concatenate the hidden units of the cmD image and HRRP image into 64 hidden units, and use two fully connected layers to ultimately transform these hidden units into an output layer with 2 units. In the calculation process, the activation functions of the convolutional layer and fully connected layer are Rectified Linear Unit (ReLU) functions, while the activation function of the output layer is Softmax function, which will be beneficial for the recognition of UAV and bird [44]. The designed low-altitude target recognition network will use a large amount of cmD and HRRP image samples for offline training in a data-driven manner. The training process will employ the cross entropy loss function and the adaptive moment estimation (Adam) optimizer. Once the network training converges, the best model will be deployed for online testing.

D. Computational Complexity Analysis

The computational complexity of the proposed scheme mainly comes from low-altitude target feature extraction and AI recognition network. In terms of feature extraction, the computational complexity of cmD feature extraction is $O\{G(MN_0^2 + M^2N_0)\}$, and the computational complexity of HRRP feature extraction is $O\{G(M^2 + MI)\}$. Different from traditional signal processing, the computational complexity of AI network is typically represented by the number of model parameters. Here the number of parameters for the proposed low-altitude target recognition network is 0.15 M, which is a lightweight network and easy to deploy on edge devices.

V. SIMULATION RESULTS

In this section, we generate a UAV and bird echo signal dataset, and then evaluate the performance of the proposed low-altitude target recognition scheme.

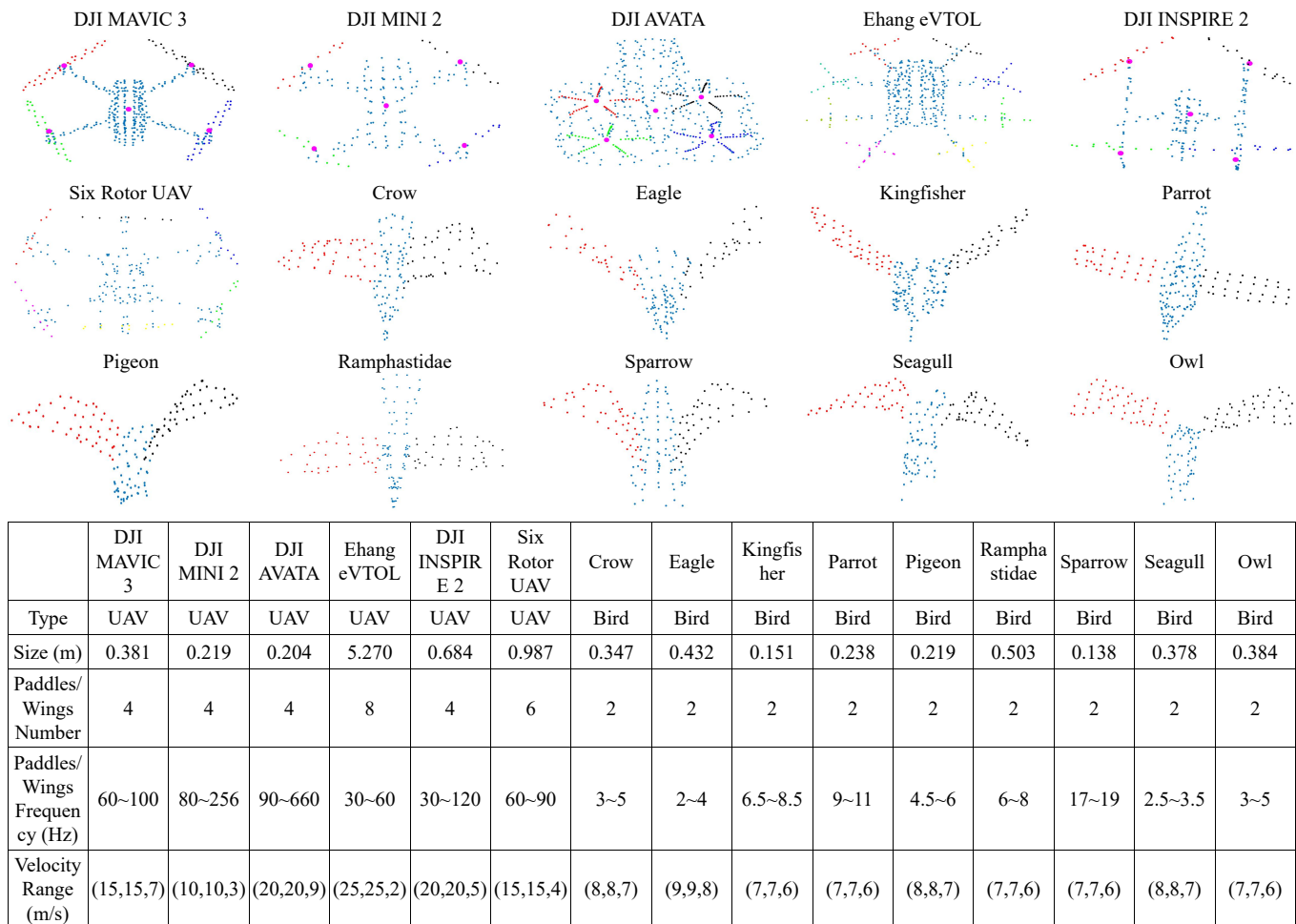


Fig. 8. Calibration point clouds and main information for 15 types of low-altitude targets.

A. UAV and Bird Echo Signal Dataset

Based on the echo signal calculation process in Section III, we first construct the CPCs for 6 types of UAVs and 9 types of birds. The UAVs include DJI MAVIC 3, DJI MINI 2, DJI AVATA, Ehang eVTOL, DJI INSPIRE 2, and Six Rotor UAV. Among them, DJI MAVIC 3, DJI MINI 2, DJI AVATA, and DJI INSPIRE 2 are four rotor UAVs; Six Rotor UAV is a six rotor UAV; and Ehang eVTOL is a eight rotor UAV. The birds include crow, eagle, kingfisher, parrot, pigeon, ramphastidae, sparrow, seagull, and owl. The CPCs and main information of these low-altitude targets are shown in Fig. 8³, in which the size of a UAV refers to the length of the diagonal of its body, the size of a bird refers to the length of its body from head to toe, the paddle frequency refers to the number of rotations of the UAV's paddle within 1 s, the wing frequency refers to the number of times a bird flaps its wings within 1 s, and the velocity range refers to the absolute value of the 3D velocity not exceeding (v_x, v_y, v_z) .

To generate the UAV and bird echo signal dataset, we set the operating frequency of BS as $f_0 = 26$ GHz, set the subcarrier spacing as $\Delta f = 480$ kHz, set the number of subcarriers as

³The information of the birds is mainly obtained through [45]–[47], and the information of the UAVs is mainly obtained through [48], [49].

$M = 4096$, set the antenna spacing as $d_x = d_z = d = \frac{\lambda}{2} = \frac{c}{2f_0}$, set the array size of HU-UPA as $N_H^x \times N_H^z = 8 \times 8$, set the array size of RU-UPA as $N_R^x \times N_R^z = 8 \times 8$, and set the OFDM symbol interval as $T_s = 10$ μ s. To fully extract the cmd and HRRP features of low-altitude target, we set the number of OFDM symbols contained in one TCF as $N = 12800$, and then the corresponding total observation duration is 0.128 s.

With these system parameters and CPCs, we generate 300 motion models corresponding to each type of UAV and 200 motion models corresponding to each type of bird by randomly changing the position, velocity, attitude, paddle frequency, wing frequency and other parameters of UAVs and birds. Then with these 3600 motion models, based on Eq. (17), Eq. (20), and Eq. (22), we finally generate a UAV and bird echo signal dataset containing 3600 noiseless echo signal matrices.

B. Data Preprocessing and Evaluation Metric for the Low-Altitude Target Recognition Network

For the data preprocessing of the low-altitude target recognition network, we add random noise with SNR belongs to $\{-20, -15, -10, -5, 0, 5, 10, 15, 20, 25, 30\}$ dB to the noiseless echo signal matrices, where each noiseless echo signal matrix independently repeats 6 times at each SNR, and

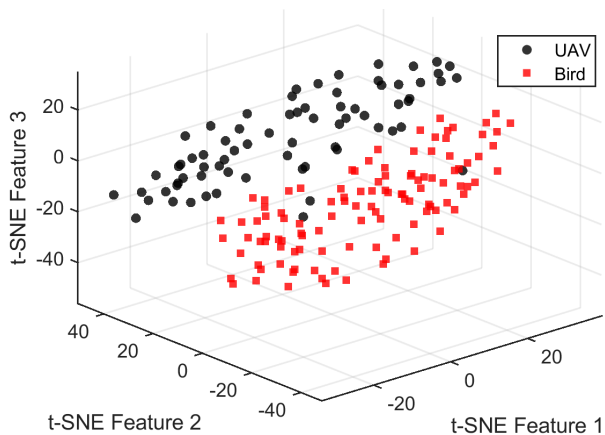


Fig. 9. t-SNE analysis on 200 randomly selected samples from 10 dB dataset.

then $3600 \times 11 \times 6 = 237600$ noisy echo signal matrices are obtained. Here based on Eq. (22), the SNR of echo signal can be defined as

$$\text{SNR} = \frac{\mathbb{E} \{ |\mathbf{w}_{n,m}^H \mathbf{H}_{n,m}^{\text{target}} \mathbf{x}_{n,m}^*|^2 \}}{\mathbb{E} \{ |n_{n,m}|^2 \}}. \quad (32)$$

Next, we set the number of groups for feature extraction as $G = 100$ with each group containing $N_0 = 128$ symbols. We set the observation range and resolution of HRRP as $[-r_{\text{HRRP,min}}, r_{\text{HRRP,max}}] = [-3m, 3m]$ and $\Delta r_{\text{HRRP}} = 0.01m$. Then we extract one cmD image and one HRRP image from each noisy echo signal matrix, where the image size is set as $3@256 \times 256$. To facilitate the storage and retrieval of the images, we concatenate the cmD image and HRRP image into an aggregated image with a size $3@512 \times 256$, which will be re-split into one mD image and one HRRP image during the data loading stage of the network. Finally, we save these 237600 aggregated images to train, validate, and evaluate the low-altitude target recognition network.

Assuming there are a total of $Z_{U,0}$ UAV image samples and $Z_{B,0}$ bird image samples, the low-altitude target recognition network recognizes $Z_{U,1}$ out of all the UAV image samples as UAV, and recognizes $Z_{B,1}$ out of all the bird image samples as bird. Then the recognition accuracy of the network can be defined as

$$\text{Acc} = \frac{Z_{U,1} + Z_{B,1}}{Z_{U,0} + Z_{B,0}}, \quad (33)$$

which will be employed as the performance evaluation metric.

C. Analysis of t-Distributed Stochastic Neighbor Embedding for cmD and HRRP

To verify the differences in cmD and HRRP features between UAVs and birds, we utilize the pre-trained ResNet-50 model to extract the deep level features from cmD and HRRP [50]. These deep level features extracted through convolutional layers and fully connected layers are high-dimensional vectors. We then utilize the t-distributed stochastic neighbor embedding (t-SNE) to reduce these high-dimensional feature vectors to 3D vectors and show them within the 3D space in Fig. 9 [51]–[53]. It can be seen that the t-SNE feature map of these deep

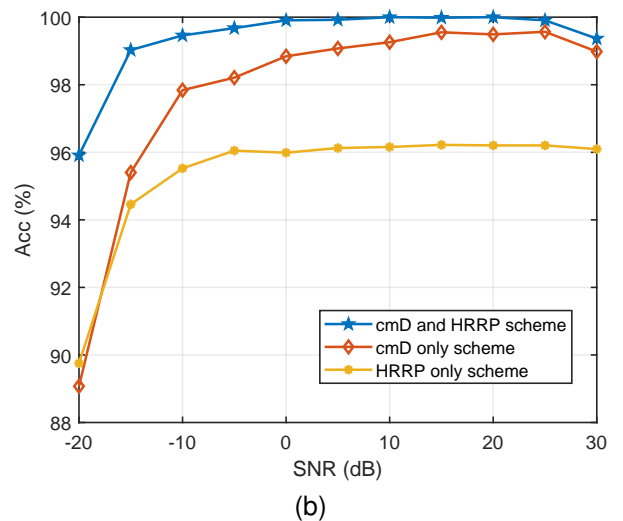
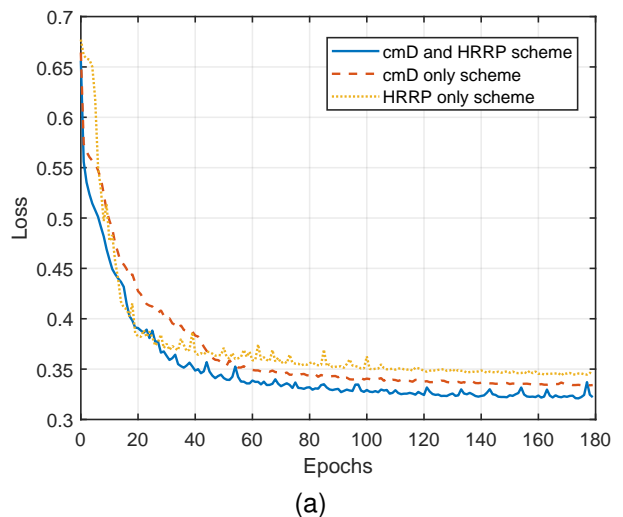


Fig. 10. Training loss and testing accuracy of low-altitude target recognition. (a) The network training loss versus training epochs of different schemes. (b) The network testing recognition accuracy versus SNR of different schemes.

level features exhibit good aggregation results, and hence cmD and HRRP can be used for the recognition of UAVs and birds.

D. Overall Accuracy of Low-Altitude Target Recognition

To conduct feature comparison, we refer to the scheme that combines cmD and HRRP features as “cmD and HRRP scheme”, refer to the scheme that only uses cmD feature as “cmD only scheme”, and refer to the scheme that only uses HRRP feature as “HRRP only scheme”. Then we select 190080, 23760, and 23760 samples from all the aggregated images as the training set, validation set, and testing set, respectively. Fig. 10 shows the training loss curve of the low-altitude target recognition network on the training set, as well as the recognition accuracy versus SNR on the testing set.

As shown in Fig. 10(a), the loss of network model gradually decreases with the increase of training epochs and eventually tends to converge. This means that the proposed low-altitude target recognition network has good convergence on dataset of UAVs and birds. Besides, it can be seen that the convergence value of cmD and HRRP scheme is lower than those of cmD

cmD and HRRP scheme															
Acc (%)	DJI MAVIC 3	DJI MINI 2	DJI AVATA	Ehang eVTOL	DJI INSPIRE 2	Six Rotor UAV	Crow	Eagle	Kingfisher	Parrot	Pigeon	Ramphastidae	Sparrow	Seagull	Owl
UAV	99.55	99.49	99.31	99.85	99.34	99.61	0.38	0.28	1.39	1.21	0.43	0.53	0.81	0.58	1.31
Bird	0.45	0.51	0.69	0.15	0.66	0.39	99.62	99.72	98.61	98.79	99.57	99.47	99.19	99.42	98.69

cmD only scheme															
Acc (%)	DJI MAVIC 3	DJI MINI 2	DJI AVATA	Ehang eVTOL	DJI INSPIRE 2	Six Rotor UAV	Crow	Eagle	Kingfisher	Parrot	Pigeon	Ramphastidae	Sparrow	Seagull	Owl
UAV	99.26	98.55	98.45	96.35	97.85	97.53	2.10	5.00	2.85	2.05	1.19	1.97	1.39	3.46	2.40
Bird	0.74	1.45	1.55	3.65	2.15	2.47	97.90	95.00	97.15	97.95	98.81	98.03	98.61	96.54	97.60

HRRP only scheme															
Acc (%)	DJI MAVIC 3	DJI MINI 2	DJI AVATA	Ehang eVTOL	DJI INSPIRE 2	Six Rotor UAV	Crow	Eagle	Kingfisher	Parrot	Pigeon	Ramphastidae	Sparrow	Seagull	Owl
UAV	98.72	99.23	96.31	98.59	95.02	94.93	0.28	1.09	0.20	0.25	0.00	0.30	0.58	16.89	38.41
Bird	1.28	0.77	3.69	1.41	4.98	5.07	99.72	98.91	99.80	99.75	100.00	99.70	99.42	83.11	61.59

Fig. 11. Confusion matrices of recognition accuracy for all types of UAVs and birds, in which the models used are the trained models in Section V-C.

Training Set: DJI MAVIC 3 + DJI MINI 2 + Crow + Eagle															
Acc (%)	DJI MAVIC 3	DJI MINI 2	DJI AVATA	Ehang eVTOL	DJI INSPIRE 2	Six Rotor UAV	Crow	Eagle	Kingfisher	Parrot	Pigeon	Ramphastidae	Sparrow	Seagull	Owl
UAV	99.97	99.93	99.56	4.49	91.21	66.78	1.44	1.06	11.79	11.82	1.87	0.96	6.94	10.56	2.12
Bird	0.03	0.07	0.44	95.51	8.79	33.22	98.56	98.94	88.21	88.18	98.13	99.04	93.06	89.44	97.88

Training Set: DJI MAVIC 3 + Ehang eVTOL + Six Rotor UAV + Crow + Eagle + Kingfisher															
Acc (%)	DJI MAVIC 3	DJI MINI 2	DJI AVATA	Ehang eVTOL	DJI INSPIRE 2	Six Rotor UAV	Crow	Eagle	Kingfisher	Parrot	Pigeon	Ramphastidae	Sparrow	Seagull	Owl
UAV	99.55	96.21	88.35	99.73	98.99	99.21	0.68	0.63	1.16	2.17	0.53	0.48	1.04	6.21	6.09
Bird	0.45	3.79	11.65	0.27	1.01	0.79	99.32	99.37	98.84	97.83	99.47	99.52	98.96	93.79	93.91

Fig. 12. Confusion matrices of recognition accuracy obtained by training models with different datasets.

only scheme and HRRP only scheme, which means that the cmD and HRRP scheme has learned more comprehensive data features from the dataset.

As shown in Fig. 10(b), the overall recognition accuracy of the trained model on the testing set gradually improves with the increase of SNR. The average accuracy of cmD and HRRP scheme, cmD only scheme, and HRRP only scheme on all SNRs are 99.37%, 97.75%, and 95.34%, respectively. The average accuracy of cmD and HRRP scheme, cmD only scheme, and HRRP only scheme for the samples below 0 dB are 98.51%, 95.13%, and 93.94%, respectively. These results confirm the effectiveness of the proposed low-altitude target recognition scheme. Besides, the overall highest accuracy of the HRRP scheme can only reach 96.21%, which means that the HRRP cannot recognize some specific targets. Meanwhile, it can be seen that in terms of overall recognition ability, the accuracy of the cmD and HRRP scheme is higher than that of the cmD only scheme, and the accuracy of the cmD only scheme is higher than that of the HRRP only scheme.

E. Accuracy for Different Types of UAVs and Birds

Based on the models trained in Section IV C, we further test the recognition accuracy of the models on different types of UAVs and birds, and the confusion matrices are shown in Fig. 11. It can be seen that the recognition accuracy of cmD and HRRP scheme on all types of low-altitude targets is above 98%. The cmD only scheme performs poorly in recognizing eagle to bird. The HRRP only scheme performs poorly in recognizing DJI INSPIRE 2 to UAV, and performs poorly in recognizing seagull and owl to bird. Importantly, Fig. 11 indicates that combining cmD and HRRP can realize better recognition performance on most types of low-altitude targets than using them alone.

F. Impact of Datasets on Recognition Generalization

We train the low-altitude target recognition network with different sub-datasets in cmD and HRRP scheme, and then the confusion matrices obtained from the converged models on the testing set are shown in Fig. 12. When the training set only includes two types of four rotor UAV, DJI MAVIC 3 and

DJI MINI 2, as well as two types of birds, crow and eagle, the recognition accuracy for Six Rotor UAV and Ehang eVTOL decrease to 66.78% and 4.49%. This indicates that the network model trained from the four rotor UAV cannot generalize to the six rotor UAV and Ehang eVTOL. Hence Fig. 12 inspires that a dataset covering most types of UAVs and birds is necessary for training the low-altitude target recognition network.

VI. CONCLUSIONS

In this paper, we proposed a UAV and bird recognition scheme for ISAC system. We formulated the motion equations and echo signals for UAVs and birds. Then we extracted the cmD spectrum and the HRRP of low-altitude targets from the echoes. Next, we designed a dual feature fusion enabled low-altitude target recognition network with CNN, which employed the images of cmD spectrum and HRRP as inputs to jointly recognize the categories of targets. Meanwhile, we generated 237600 cmD and HRRP image samples to train, validate, and evaluate the designed low-altitude target recognition network. The simulation results confirmed the effectiveness of the proposed scheme.

REFERENCES

- [1] H. Huang, J. Su, and F.-Y. Wang, "The potential of low-altitude airspace: The future of urban air transportation," *IEEE Trans. Intell. Veh.*, vol. 9, no. 8, pp. 5250–5254, Aug. 2024.
- [2] B. Zheng and F. Liu, "Random signal design for joint communication and SAR imaging towards low-altitude economy," *IEEE Wireless Commun. Lett.*, vol. 13, no. 10, pp. 2662–2666, Oct. 2024.
- [3] C. Huang, S. Fang, H. Wu, Y. Wang, and Y. Yang, "Low-altitude intelligent transportation: System architecture, infrastructure, and key technologies," *J. Ind. Inf. Integr.*, vol. 42, p. 100694, Nov. 2024.
- [4] Y. Jiang *et al.*, "6G non-terrestrial networks enabled low-altitude economy: Opportunities and challenges," *arXiv e-prints*, p. arXiv:2311.09047, Nov. 2023.
- [5] S. Xiang, A. Xie, M. Ye, X. Yan, X. Han, H. Niu, Q. Li, and H. Huang, "Autonomous eVTOL: A summary of researches and challenges," *Green Energy Intell. Transp.*, vol. 3, no. 1, p. 100140, Feb. 2024.
- [6] S. H. Alsamhi, O. Ma, M. S. Ansari, and F. A. Almalki, "Survey on collaborative smart drones and internet of things for improving smartness of smart cities," *IEEE Access*, vol. 7, pp. 128125–128152, Aug. 2019.
- [7] M. A. Hoque *et al.*, "IoTaaS: drone-based internet of things as a service framework for smart cities," *IEEE Internet Things J.*, vol. 9, no. 14, pp. 12425–12439, Jul. 2022.
- [8] S. H. Alsamhi *et al.*, "Collaboration of drone and internet of public safety things in smart cities: An overview of QoS and network performance optimization," *Drones*, vol. 3, no. 1, Jan. 2019.
- [9] A. Fotouhi *et al.*, "Survey on UAV cellular communications: Practical aspects, standardization advancements, regulation, and security challenges," *IEEE Commun. Surv. Tutor.*, vol. 21, no. 4, pp. 3417–3442, Mar. 2019.
- [10] S. Javaid, N. Saeed, Z. Qadir, H. Fahim, B. He, H. Song, and M. Bilal, "Communication and control in collaborative UAVs: recent advances and future trends," *IEEE Trans. Intell. Trans. Sys.*, vol. 24, no. 6, pp. 5719–5739, Jun. 2023.
- [11] F. Liu, Y. Cui, C. Masouros, J. Xu, T. X. Han, Y. C. Eldar, and S. Buzzi, "Integrated sensing and communications: Toward dual-functional wireless networks for 6G and beyond," *IEEE J. Sel. Areas Commun.*, vol. 40, no. 6, pp. 1728–1767, Jun. 2022.
- [12] H. Luo, T. Zhang, C. Zhao, Y. Wang, B. Lin, Y. Jiang, D. Luo, and F. Gao, "Integrated sensing and communications framework for 6G networks," *arXiv e-prints*, p. arXiv:2405.19925, May 2024.
- [13] M. Giordani, M. Polese, M. Mezzavilla, S. Rangan, and M. Zorzi, "Toward 6G networks: Use cases and technologies," *IEEE Commun. Mag.*, vol. 58, no. 3, pp. 55–61, Mar. 2020.
- [14] Y. Cui, F. Liu, X. Jing, and J. Mu, "Integrating sensing and communications for ubiquitous IoT: Applications, trends, and challenges," *IEEE Netw.*, vol. 35, no. 5, pp. 158–167, Nov. 2021.
- [15] ITU, "Future technology trends of terrestrial international mobile telecommunications systems towards 2030 and beyond," 2022.
- [16] Z. Xiao *et al.*, "A novel joint angle-range-velocity estimation method for MIMO-OFDM ISAC systems," *IEEE Trans. Signal Process.*, vol. 72, pp. 3805–3818, Aug. 2024.
- [17] X. Lu, Z. Wei, R. Xu, L. Wang, B. Lu, and J. Piao, "Integrated sensing and communication enabled multiple base stations cooperative UAV detection," *arXiv e-prints*, p. arXiv:2404.12705, Apr. 2024.
- [18] R. Liu, M. Jian, D. Chen, X. Lin, Y. Cheng, W. Cheng, and S. Chen, "Integrated sensing and communication based outdoor multi-target detection, tracking, and localization in practical 5G networks," *Intell. Converged Netw.*, vol. 4, no. 3, pp. 261–272, Sep. 2023.
- [19] R. Li, Q. Zhang, D. Ma, K. Yu, and Y. Huang, "Joint target assignment and resource allocation for multi-base station cooperative ISAC in UAV detection," *IEEE Trans. Veh. Technol.*, pp. 1–15, Jan. 2025.
- [20] J. Wei, D. Ma, F. He, Q. Zhang, Z. Feng, Z. Liu, and T. Liang, "UAV's rotor micro-Doppler feature extraction using integrated sensing and communication signal: Algorithm design and testbed evaluation," *arXiv e-prints*, p. arXiv:2408.16415, Aug. 2024.
- [21] D. Ma *et al.*, "Performance evaluation of micro-Doppler based UAV identification using different 5G frame structures," in *Proc. 2nd Int. Conf. Mobile Internet, Cloud Comput. Inf. Security*, Changsha City, China, Apr. 2024, pp. 173–179.
- [22] N. Mohajerin *et al.*, "Feature extraction and radar track classification for detecting UAVs in civilian airspace," in *Proc. IEEE Radar Conf.*, Cincinnati, OH, USA, May 2014, pp. 674–679.
- [23] X. Zhang, V. Mehta, M. Bolic, and I. Mantegh, "Hybrid AI-enabled method for UAS and bird detection and classification," in *Proc. IEEE Int. Conf. Syst.*, Toronto, ON, Canada, Oct. 2020, pp. 2803–2807.
- [24] Jochumsen *et al.*, "Recursive bayesian classification of surveillance radar tracks based on kinematic with temporal dynamics and static features," in *Proc. Int. Radar Conf.*, Lille, France, Oct. 2014, pp. 1–6.
- [25] Doumard *et al.*, "Radar discrimination of small airborne targets through kinematic features and machine learning," in *Proc. IEEE/AIAA 41st Digital Avionics Syst. Conf.*, Portsmouth, VA, USA, Sep. 2022, pp. 1–10.
- [26] C. Bennett *et al.*, "Use of symmetrical peak extraction in drone micro-Doppler classification for staring radar," in *Proc. IEEE Radar Conf.*, Florence, Italy, Sep. 2020, pp. 1–6.
- [27] H. Dale *et al.*, "A comparison of convolutional neural networks for low SNR radar classification of drones," in *Proc. IEEE Radar Conf.*, Atlanta, GA, USA, May 2021, pp. 1–5.
- [28] S. Rahman and D. A. Robertson, "Multiple drone classification using millimeter-wave CW radar micro-Doppler data," in *Proc. Radar Sensor Technol. XXIV*, vol. 11408, Apr. 2020, SPIE.
- [29] B.-S. Oh, X. Guo, F. Wan, K.-A. Toh, and Z. Lin, "Micro-Doppler mini-UAV classification using empirical-mode decomposition features," *IEEE Geosci. and Remote Sens. Lett.*, vol. 15, no. 2, pp. 227–231, Dec. 2018.
- [30] L. Du, H. Liu, and Z. Bao, "Radar HRRP statistical recognition: Parametric model and model selection," *IEEE Trans. Signal Process.*, vol. 56, no. 5, pp. 1931–1944, May 2008.
- [31] L. Du, P. Wang, H. Liu, M. Pan, F. Chen, and Z. Bao, "Bayesian spatiotemporal multitask learning for radar HRRP target recognition," *IEEE Trans. Signal Process.*, vol. 59, no. 7, pp. 3182–3196, Jul. 2011.
- [32] L. Du, H. Liu, Z. Bao, and J. Zhang, "A two-distribution compounded statistical model for radar hrrp target recognition," *IEEE Trans. Signal Process.*, vol. 54, no. 6, pp. 2226–2238, Jun. 2006.
- [33] W. Jiang, Z. Liu, Y. Wang, Y. Lin, Y. Li, and F. Bi, "Realizing small UAV targets recognition via multi-dimensional feature fusion of high-resolution radar," *Remote Sens.*, vol. 16, no. 15, Jul. 2024.
- [34] Z. Gao, Z. Wan, D. Zheng, S. Tan, C. Masouros, D. W. K. Ng, and S. Chen, "Integrated sensing and communication with mmWave massive MIMO: A compressed sampling perspective," *IEEE Trans. Wireless Commun.*, vol. 22, no. 3, pp. 1745–1762, Mar. 2023.
- [35] J. Chen, Y.-c. Wu, S. Ma, and T.-s. Ng, "MI joint CFO and channel estimation in OFDM systems with timing ambiguity," *IEEE Trans. Wireless Commun.*, vol. 7, no. 7, pp. 2436–2440, Jul. 2008.
- [36] Z. Du, F. Liu, W. Yuan, C. Masouros, Z. Zhang, S. Xia, and G. Caire, "Integrated sensing and communications for V2I networks: Dynamic predictive beamforming for extended vehicle targets," *IEEE Trans. Wireless Commun.*, vol. 22, no. 6, pp. 3612–3627, Jun. 2023.
- [37] R. Shafin, L. Liu, J. Zhang, and Y.-C. Wu, "DoA estimation and capacity analysis for 3-D millimeter wave massive-MIMO/FD-MIMO OFDM systems," *IEEE Trans. Wireless Commun.*, vol. 15, no. 10, pp. 6963–6978, Oct. 2016.
- [38] W. Wang and W. Zhang, "Jittering effects analysis and beam training design for UAV millimeter wave communications," *IEEE Trans. Wireless Commun.*, vol. 21, no. 5, pp. 3131–3146, Oct. 2022.

- [39] H. Luo, Y. Wang, D. Luo, J. Zhao, H. Wu, S. Ma, and F. Gao, "Integrated sensing and communications in clutter environment," *IEEE Trans. Wireless Commun.*, pp. 1–1, Mar. 2024.
- [40] H. Luo, F. Gao, F. Liu, and S. Jin, "6D motion parameters estimation in monostatic integrated sensing and communications system," *IEEE Trans. Commun.*, pp. 1–1, Jan. 2025.
- [41] P. Cignoni *et al.*, "MeshLab: an open-source mesh processing tool," in *Proc. Eurographics Italian Chapter Conf.*, The Eurographics Association, Jul. 2008.
- [42] N. Dyn, D. Levine, and J. A. Gregory, "A butterfly subdivision scheme for surface interpolation with tension control," *ACM Trans. Graph.*, vol. 9, no. 2, pp. 160–169, Apr. 1990.
- [43] J. S. Dai, "Euler–rodrigues formula variations, quaternion conjugation and intrinsic connections," *Mech. Mach. Theory*, vol. 92, pp. 144–152, Oct. 2015.
- [44] Y. LeCun, L. Bottou, Y. Bengio, and P. Haffner, "Gradient-based learning applied to document recognition," *Proc. IEEE*, vol. 86, no. 11, pp. 2278–2324, Nov. 1998.
- [45] C. J. Pennycuick, "Speeds and wingbeat frequencies of migrating birds compared with calculated benchmarks," *Journal of Experimental Biology*, vol. 204, pp. 3283–3294, 10 2001.
- [46] K. Krishnan *et al.*, "The role of wingbeat frequency and amplitude in flight power," *Journal of The Royal Society Interface*, vol. 19, no. 193, p. 20220168, 2022.
- [47] C. J. Pennycuick, "Wingbeat frequency of birds in steady cruising flight: New data and improved predictions," *Journal of Experimental Biology*, vol. 199, pp. 1613–1618, 07 1996.
- [48] H. Dale, M. Jahangir, C. J. Baker, M. Antoniou, S. Harman, and B. I. Ahmad, "Convolutional neural networks for robust classification of drones," in *2022 IEEE Radar Conference (RadarConf22)*, pp. 1–6, 2022.
- [49] DJI, "Dji website." <https://www.dji.com/cn>. [Online; accessed 2025].
- [50] K. He, X. Zhang, S. Ren, and J. Sun, "Deep residual learning for image recognition," in *Proc. IEEE Conf. Comput. Vis. Pattern Recognit.*, pp. 770–778, 2016.
- [51] G. E. Hinton and S. Roweis, "Stochastic neighbor embedding," in *Proc. Adv. Neural Inf. Process. Syst.* (S. Becker, S. Thrun, and K. Obermayer, eds.), vol. 15, MIT Press, 2002.
- [52] H. Luo, J. Liu, S. Wu, Z. Nie, H. Li, and J. Wu, "A semi-supervised deception jamming discrimination method," in *Proc. IEEE 7th Int. Conf. Cloud Comp. Intell. Sys.*, Xi'an, China, Nov. 2021, pp. 428–432.
- [53] L. Van der Maaten and G. Hinton, "Visualizing data using t-SNE," *J. Mach. Learn. Res.*, vol. 9, no. 11, Nov. 2008.